IEEE Access
Multidisciplinary | Rapid Review | Open Access Journal

Received May 9, 2019, accepted May 23, 2019, date of publication May 29, 2019, date of current version December 31, 2019.

Digital Object Identifier 10.1109/ACCESS.2019.2919682

Visual Texture-Based 3-D Roughness Measurement for Additive Manufacturing Surfaces

HAOTIAN YU, CHONGCHONG PENG, ZHUANG ZHAO, LIANFA BAI, AND JING HAN

Jiangsu Key Laboratory of Spectral Imaging and Intelligent Sense, Nanjing University of Science and Technology, Nanjing 210094, China

Corresponding author: Jing Han (eohj@njust.edu.cn)

This work was supported by the National Natural Science Foundation of China under Grant 61727802.

ABSTRACT In this paper, for evaluating the 3-D roughness of the additive manufacturing surfaces, we constructed a 3-D reconstruction system of structured light scanner. By calibrating the system, the center line of structured light is extracted online to reconstruct the profile of additive manufacturing and realize data registration. A dynamic texture coarseness algorithm is proposed, which combines 3-D data with 2-D Gaussian filtering and texture coarseness characteristics to transform 3-D roughness into visual image texture coarseness. The algorithm is applied to evaluate 3-D weld roughness with low delay. The validity of the algorithm is verified by roughness comparison specimens and the actual material adding experiment. The result of roughness is reliable and conforms to the evaluation standard of weld quality. At the same time, the position of structured light is optimized in the process of on-line detection, which reduces the complexity of extracting contour centerline and ensures the low delay characteristic of roughness calculation.

INDEX TERMS 3-D reconstruction, dynamic texture coarseness, 3-D roughness of additive manufacturing.

I. INTRODUCTION

Weld forming is an important index to measure welding quality, and the surface roughness information of weld is the first part to be concerned. The evaluation of surface roughness of workpieces such as welding and material addition can be divided into two categories: qualitative and quantitative. The qualitative description is based on artificial vision and tactile comparison of the workpiece surface and the roughness comparison specimens to obtain a rough roughness level [1]. Quantitative evaluation methods mainly include light-cutting method (parts with low precision requirements for light-cutting microscope measurement) [2], [3]; interferometry (interference microscope light wave interference modulation produces bending to reflect the surface roughness of the tested part) [4], [5]; stylus method (stylus profiler) [6], [7].

In the traditional judgment method, the light cutting method and the interference method cannot realize on-line surface roughness determination due to the limitation of equipment and principle. The most widely used method is stylus, but in the measurement process, the stylus needs to contact the measured surface directly. None of these methods can meet the technical requirements of non-contact, online work and high precision in the field of welding quality monitoring at the same time. In order to realize the automation, intellectualization and accuracy of inspection, many studies on welding quality monitoring are based on visual sensing system. Machine vision can be used for real-time detection and online control of product quality in automated welding process [8]–[12]. However, most of the current studies on weld quality analysis are to detect the specific welding defect, such as undercut [13], overlap [14], slag [15], and lack of automatic control of the overall quality of the weld area.

Laser vision system is one of the most efficient and adaptable seam sensor systems at present. In this paper, the real 3-D data information of weld surface is obtained by scanning with the line structured light system following the welding robot. Based on the roughness of mechanical field and the coarseness of Tamura [16], a new dynamic texture coarseness (DTC) algorithm was proposed. This algorithm is used to quantitatively evaluate the surface roughness of welding seam area. At the same time, we explored the optimal assembly distance of structured light device relative to the welding robot torch, so as to provides an important reference for the intelligent detection of weld quality and online parameter

The associate editor coordinating the review of this manuscript and approving it for publication was Yong Yang.

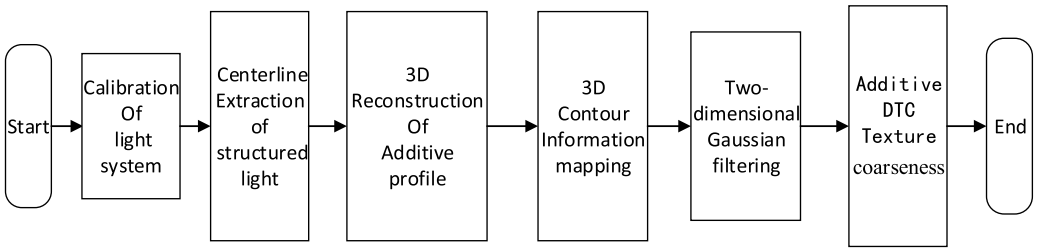

FIGURE 1. Measuring scheme of surface roughness of additive Manufacturing.

correction. In this paper, the scanning device follows the welding system, which can achieve non-destructive testing without re-sampling the target.

II. 3-D ROUGHNESS MEASUREMENT SCHEME

To the best of our knowledge, there are no researchers focused on the research of 3-D roughness based on visual texture. In this part, we illustrate our research from the measurement program and 3-D reconstruction system.

A. 3-D ROUGHNESS MEASUREMENT PROGRAM FOR ADDITIVE MANUFACTURING

At present, the evaluation criteria for 2-D surface contours have been completed. However, with the development of processing technology and the diversification of materials, the surface of the workpiece is affected by many factors and its texture features are more and more complicated. The evaluation method of 2-D surface contour can no longer meet the demand, and the maturity of 3-D evaluation is urgently needed. International standards for 3-D surface parameters are being developed [17], [18], and no unified standard has been formed. The surface roughness of the additive is the change of the 3-D contour information of the surface of the structural member, and the texture coarseness is mainly used to evaluate the 2-D texture distribution of the object in the image. The quality detection system of the roughness of the additive surface proposed in this paper is affected by the visual texture. Inspired, a dynamic texture coarseness algorithm is proposed for online quality analysis of the 3-D surface roughness.

As shown in Fig. 1, we need to calibrate the 3-D reconstruction system of structure light, including camera calibration, plane calibration of structured light and hand-eye calibration of robot. Using the calibration results, we can reconstruct and stitch the 3-D information of the extracted central light strip of structured light. Then, we can map the depth information of the obtained contour data of the additive and obtain the depth information after Gaussian filtering. At last, the DTC algorithm is used to calculate the dynamic texture coarseness of the data to detect the surface roughness information of the target material.

B. 3-D RECONSTRUCTION BASED ON LINE STRUCTURED LIGHT

Optical 3D measurement is widely used in many fields such as industrial automatic inspection, product quality control, cultural relics reproduction [19]. As additive manufacturing is becoming an important carrier for the country to realize the return of manufacturing, optical 3D measurement also has developed as a fundamental capability for robots over the past decades [20], therefore Simultaneous Localization and Mapping (SLAM) is a fundamental step for many robotic applications. It concurrently estimates robot poses and reconstructs traversed environment models. Many effective SLAM algorithms using visual sensors, such as monocular or stereo cameras [21], [22] and RGB-D cameras [23]–[25], have been proposed over the past years. Many industries have benefited from the development of the SLAM technology. In addition, Structure from Motion (SfM) is also an important means of 3D reconstruction, the goal of SfM is to automatically recover camera motion and scene structure using two scenes or multiple scenes. It is a self-calibrating technology that automatically performs camera tracking and motion matching. The incremental SfM method [26]–[28] is currently the most widely used method. A basic SfM pipeline can be described as: detecting feature points for each picture, matching feature points in each pair of pictures, retaining only matching that satisfies geometric constraints, and finally performing an iterative, robust SfM method restores the camera's intrinsic parameters and extrinsic parameters.

The 3-D reconstruction methods mentioned above are well applied in many robot scenes, but in the field of welding and additive manufacturing, there are various spatters, smoke and dust, strong arc light interference in the working process, the harshness and complexity of the environment make ordinary 3-D reconstruction methods unable to meet the needs of on-site operations. Also because of the measurement requirement of sub-millimeter precision, we have chosen the structured light reconstruction scheme, as the poor anti-interference and real-time performance of the planar array structured light, we use laser scanning method to project line structured light to the measured object, then the shape data of the measured object is calculated from the image carrying the 3-D profile information of the object to be measured. The physical device diagram of the laser scanning sensor system used in this paper are shown in Fig. 2. The device is mainly composed of a camera and a line laser. Line laser projected onto the motherboard reflects the profile information of the weld cross-section, and the camera collects the image of line laser cutting profile for 3-D reconstruction.

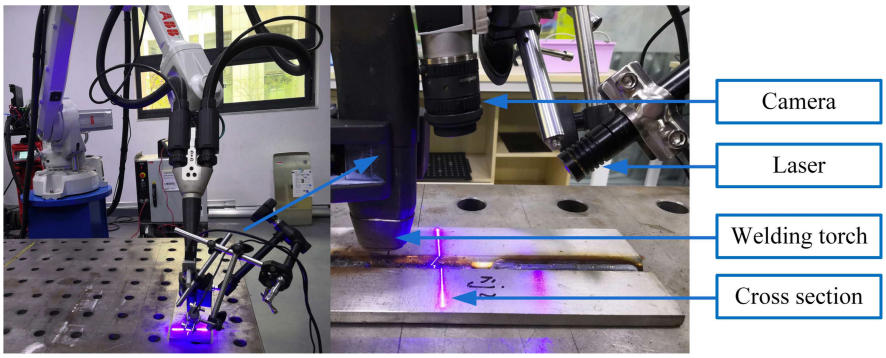

FIGURE 2. The physical device diagram of the laser scanning sensor system.

TABLE 1. Measurement error of 3-D scanning.

Error(mm)	3mm	5mm	7mm	9mm	11mm	13mm	15mm
1	0.0547	0.0527	0.0048	0.0271	0.0023	0.0533	0.0230
2	0.0535	0.0311	0.0497	0.0624	0.0468	0.0560	0.0225
3	0.0055	0.0591	0.0499	0.0307	0.0080	0.0079	0.0235
4	0.0548	0.0584	0.0012	0.0539	0.0506	0.0070	0.0339
5	0.0556	0.0637	0.0481	0.0606	0.0095	0.0180	0.0300
6	0.0055	0.0149	0.0515	0.0565	0.0023	0.0109	0.0236
7	0.0085	0.0143	0.0023	0.0612	0.0569	0.0265	0.0102
8	0.0015	0.0242	0.0536	0.0579	0.0501	0.0272	0.0688
9	0.0035	0.0348	0.0618	0.0329	0.0571	0.0299	0.0330
10	0.0634	0.0618	0.0559	0.0563	0.0166	0.0572	0.0258
11	0.0587	0.0594	0.0010	0.0566	0.0118	0.0177	0.0201
12	0.0586	0.0340	0.0538	0.0581	0.0044	0.0183	0.0207

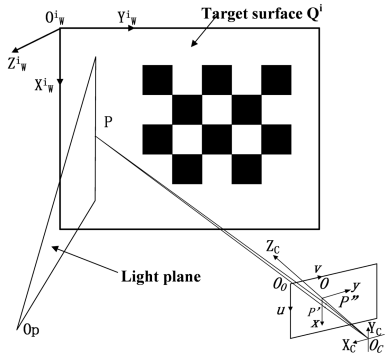

FIGURE 3. The imaging model of line structured light.

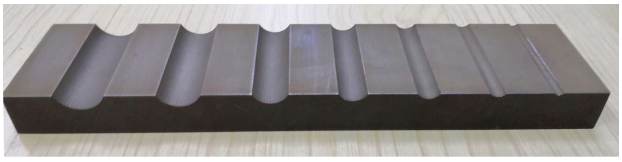

FIGURE 4. Standard concave surface workpiece.

In this paper, Zhang's calibration [29] method based on checkerboard is used to calibrate the camera to obtain camera parameters, and the least squares method [30] is used to calibrate the light plane parameters. The light plane calibration is based on the classical camera imaging model to determine the spatial position of the center points of the light strip coplanar with the target in the camera coordinate system. The mathematical model of the line structured light is shown in Fig. 3, The parameters of the light plane are calculated by using the 3-D coordinates of the calibration points in the figure, the position relationship of the plane in the camera coordinate system is described, and the parameters of the plane equation are solved.

At present, there is no corresponding international standard for line structured light measurement [31]. In this paper, the accuracy of light plane calibration is evaluated by using the standard ingots shown below.

The width of the sides of arc is 3, 5, 7, 9, 11, 13 and 15 mm in turn. The surface of the standard part is measured by the scanning device in this paper. The absolute difference between the measured value and the true width is obtained by multiple scanning calculations as shown in Table 1.

From multiple sets and multiple measurements in this table, it can be seen that the maximum error of the 3-D reconstruction system is 0.0688mm, which does not exceed 0.1 mm, and meets the requirements for measurement accuracy within 0.20 mm in the Key Special Projects of Additive Manufacturing and Laser Manufacturing.

III. ADDITIVE SURFACE ROUGHNESS ALGORITHM BASED ON GAUSSIAN FILTERING AND TEXTURE COARSENESS

A. GAUSSIAN FILTERING BASED 3-D DATUM EXTRACTION

In the characterization of 2-D surface topography, the midline is the baseline of profile evaluation, which is the basis of roughness parameter calculation. The international standard ISO 11562 specifies the extraction of surface contour reference lines with a one-dimensional Gaussian filter. The one-dimensional Gaussian weight function is formulated as:

$$h(t) = \frac{1}{\alpha\lambda_c}\exp(-\pi(\frac{t}{\alpha\lambda_c})^2) \tag{1}$$

where t is a spatial domain variable, and λ_c is the cutoff wavelength. The Fourier transform is used to obtain the amplitude transmission characteristics as shown in (2):

$$H(\Omega) = \exp(-\pi(\frac{a\Omega}{\Omega_c})^2) \tag{2}$$

when $\lambda = \lambda_c$, $H(\Omega) = 0.5$, that is, the amplitude transmission characteristic of the Gaussian filter is 50%.at this time,

$$\alpha = \sqrt{\frac{\log 2}{\pi}} = 0.4697 \tag{3}$$

Then in the measurement of 3-D surface roughness, the first thing to be determined is the datum plane. Extending the one-dimensional Gaussian filter to two-dimensional, the 2-D Gaussian function can be used to extract the 3-D surface contour datum. For the digital system, the actual measured surface contour is discrete data. $h_{i,j}$ is defined as 3-D discrete sampling data and $w_{1i,j}$ is a Gaussian datum plane, and the Gaussian formula with discrete finite is as follows:

$$w_{1i,j} = \sum_{k=-M}^{M}\sum_{l=-N}^{N} h_{i-k,j-l}g_{k,l}\Delta x\Delta y \quad i = M,\ldots,LX-M;\ j = N,\ldots,LY-N \tag{4}$$

where

$$g_{k,l} = \frac{1}{\alpha^2\lambda_{xc}\lambda_{yc}}\exp(-\pi((\frac{k\Delta x}{\alpha\lambda_{xc}})^2 + (\frac{l\Delta y}{\alpha\lambda_{yc}})^2))) \tag{5}$$

λ_{xc} and λ_{yc} are the cutoff wavelengths in the x and y directions, respectively, which can be set according to the international standard of 2-D roughness. In this paper, $\lambda_{xc} = \lambda_{yc} = 0.8mm$, $\alpha = 0.4697$.x and y are the sampling intervals,LX and LY are the data sampling points, $h_{i,j}$ is the 3-D discrete sampling data, reflecting the fluctuation of the weld surface profile.

B. DTC ALGORITHM

Based on the psychological research of visual perception of texture, Tamura proposed the expression of texture features. The six components of the Tamura texture feature correspond to the six properties of the texture feature in the psychological perspective, namely, coarseness, contrast, directionality, linearity, regularity and roughness. Coarseness is the physical quantity describing the size and distribution of grain size in texture, and it is the most basic and important texture feature. The larger the texture primitive size, the larger the span between primitives and the coarser the texture.

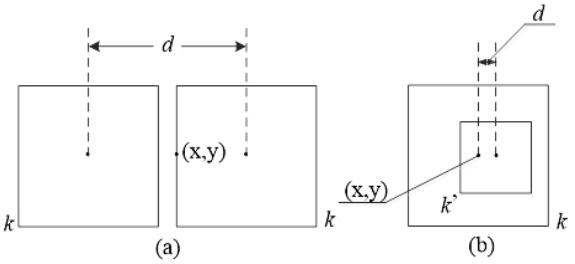

FIGURE 5. Difference windows selection method. (a) The difference windows of the DTC. (b) The difference windows of the Tamura.

As shown in Fig. 5(a), in Tamura coarseness algorithm, adjacent windows which do not overlap each other are selected to make difference, and the window size is the same. It can be seen that Tamura algorithm is suitable for extracting the texture roughness of the entire image or larger image blocks, but cannot dynamically represent the local roughness of the weld surface. This paper proposes a DTC algorithm with better universality and better noise robustness. As shown in Fig. 5(b), the DTC algorithm improves the difference window. The two windows are eccentric overlapping windows, and the window size is deviated, so that the local texture coarseness can be accurately measured.

The DTC algorithm is implemented as follows:

1) Calculate the average intensity values of pixels in the active window of size $4k\times4k$ in the image.

$$A_k(x,y) = \sum_{i=x-2k}^{x+2k-1}\sum_{j=y-2k}^{y+2k-1} f(i,j)/(4k)^2 \tag{6}$$

where k=1,2,…,$Lmax$, $Lmax$ is the maximum window scale;$f(i, j)$ is the pixel intensity value at (i, j); when $k = 0$, 3×3 window is selected.

2) For each pixel, calculate its average intensity difference between the windows in the horizontal and vertical directions, respectively.

$$E_{k,h}(x,y) = |A_{k'}(x+\rho,y) - A_k(x,y)| \tag{7}$$

$$E_{k,v}(x,y) = |A_{k'}(x,y+\rho) - A_k(x,y)| \tag{8}$$

where k'= max(k-L_b ,0), L_b is the deviation ratio of two windows; $L_b = L_{max} - \alpha$, $L_b \geq 1$, α takes the following values: $\alpha = 3$, $L_{max} \geq 5$; $\alpha = min(2, L_{max}-1)$, $L_{max} < 5$; ρ is the eccentricity of two windows, $\rho = 2k'+1$.

3) Calculate the optimal size of each pixel S_{best}.

$$S_{boxt} = 4k_{\max} \tag{9}$$

$$E_k = \max\left(E_{k,h}, E_{k,v}\right) \tag{10}$$

$$E_{\max} = \max\left(E_k\right), \quad E_{\min} = \min\left(E_k\right) \tag{11}$$

In (9), the k value is determined as follows: texture boundary points, larger and smaller texture primitive interior points.

(i) When $k = 0$, if $E_k > t_M$, terminates the judgment and $k_{max} = 0$; t_M takes the mean of the local non-zero maxima of all the E_0 pixel points, which corresponds to the texture boundary point. Otherwise, it is transferred into (ii);
(ii) Let $DE_k = |E_k - E_{k-1}|$, if Numel($DE_k < \tau_0$) = $L_{max} - 1$ and $E_k < t_m$, then $k_{max} = L_{max}$; this case corresponds to the interior points of larger texture primitives; τ_0, t_m are small positive values; experiments on a large number of texture images show that their values are all related to $\bar{E}_{min}$, $\bar{E}_{min}$*is* the average value of E_{min}, in practical applications, this paper takes $\tau_0 = \bar{E}_{min}/1.5$, $t_m = 1.8 \times E_{min}$, Otherwise, it is transferred into (iii);
(iii) k_{max}=*argmax*(E_k), this case corresponds to the interior points of smaller size texture primitives.

4) Calculate the local coarseness of the pixel based on the optimal size of each pixel in the image, and the mean of all S_{best} is used as the roughness of the whole image.

$$F_{crs} = \frac{1}{M \times N} \sum_{x=1}^{M} \sum_{y=1}^{N} S_{bett}(x, y)^{\gamma} \tag{12}$$

In order to increase the contrast, power conversion is performed on S_{best}, where $\gamma > 1$. In this paper, γ takes reference value 2.5 to improve the sensitivity to roughness.

In the process of image acquisition and propagation. The roughness algorithm proposed in the paper is applied to the actual welding and additive manufacturing. Therefore, the noise robustness of the algorithm must be considered. In fact, by (6), (7) and (8), a and b are the intensity difference after the mean filtering of the original image. In theory, the algorithm should have good anti-noise ability.

Considering specifically the influence of additive noise $n(i, j)$ the intensity value $f(i, j)$ at image pixel (i, j) becomes: $g(i, j) = f(i, j) + n(i, j)$. From (7):

$$\begin{aligned} E_{k,h} &= |\frac{1}{N_{k'}} \sum_{(i,j)\in A_{k'}} g(i,j) - \frac{1}{N_k} \sum_{(i,j)\in A_k} g(i,j)| \\ &= |\frac{1}{N_{k'}} \sum_{(i,j)\in A_{k'}} f(i,j) - \frac{1}{N_k} \sum_{(i,j)\in A_k} f(i,j) \\ &\quad + \frac{1}{N_{k'}} \sum_{(i,j)\in A_{k'}} n(i,j) - \frac{1}{N_k} \sum_{(i,j)\in A_k} n(i,j)| \end{aligned} \tag{13}$$

N_k is the total number of pixels in the window area A_k. When the areas A_k and $A_{k'}$ are all within the same texture primitive, the formula above becomes:

$$E_{k,h} = |\frac{1}{N_{k'}} \sum_{(i,j)\in A_{k'}} n(i,j) - \frac{1}{N_k} \sum_{(i,j)\in A_k} n(i,j)| \tag{14}$$

when the probability distribution radius r of $n(i, j)$, is small, the condition a:$N_k, N_{k'} \gg r$ is satisfied. By the Khinchine law of large numbers [32]: In the practice of measuring random physical quantities, the arithmetic mean of a large number of measured values is stable, close to mathematical expectation.

$$\lim_{N\to\infty} P\left\{\left|\frac{1}{N}\sum_{i=1}^{N} a_i - \mu\right| < \varepsilon\right\} = 1 \tag{15}$$

we can see that:

$$\frac{1}{N_{k'}} \sum_{(i,j)\in A_{k'}} n(i,j) \approx \mu_n, \quad \frac{1}{N_k} \sum_{(i,j)\in A_k} n(i,j) \approx \mu_n \tag{16}$$

where μ_n is the mean of the noise $n(i, j)$. Therefore (14) becomes:

$$E_{k,h} \approx 0 \tag{17a}$$

from (10):

$$E_k \approx 0, \quad or\ E_k < t_m \tag{17b}$$

where t_m is a small positive number. When the condition a: is satisfied, the (13) can be written as:

$$E_{k,h} \approx |\frac{1}{N_{k'}} \sum_{(i,j)\in A_{k'}} f(i,j) - \frac{1}{N_k} \sum_{(i,j)\in A_k} f(i,j)| \tag{18a}$$

$$E_{k,v} \approx |\frac{1}{N_{k'}} \sum_{(i,j)\in A_{k'}} f(i,j) - \frac{1}{N_k} \sum_{(i,j)\in A_k} f(i,j)| \tag{18b}$$

obviously, the larger N_k is, the better the condition a is satisfied, and the better the effect of suppressing noise. However, if the window is larger, a wider texture boundary will be produced. Considering the acceptable width of the texture boundary, when $k = 0$, the window is set to 3×3 size. Experiments show that the 3×3 window can better suppress the noise.

The texture image can be regarded as composed of different texture primitives arranged in a certain regularity. The pixels in the image can be divided into texture boundary points and texture primitive internal points.

For the inner points of the texture primitive, when the current window size k is smaller than the size of texture primitive, E_k satisfies (17b); when k crosses the size, by (10) and (18), obviously $E_k \geq 0$, the maximum value E_{max} appears. At this time, $k_{max} = k$; when the size of primitive is large, E_k are very small and the value are similar; at this time, $k_{max} = L_{max}$, the constraint condition is Numel($DE_k < \tau_0$) = $L_{max} - 1$ and $E_k < t_m$.

For the boundary point, E_k is larger, $E_k >> 0$. This is because for the boundary point, the two windows span different texture primitives, and the two items on the right side of (18a) and (18b) cannot be eliminated. Set $k_{max} = 0$ at the boundary point.

Because E_0 contains the original texture boundary information, the boundary points are judged by condition $E_0 > t_M$, t_M, takes the mean of local non-zero maxima of all pixels in E_0, and $k = 0$, $E_0 < t_m << t_M$ are obtained by formula (17c), so the interior points of texture primitives affected by noise can be effectively distinguished from the boundary points.

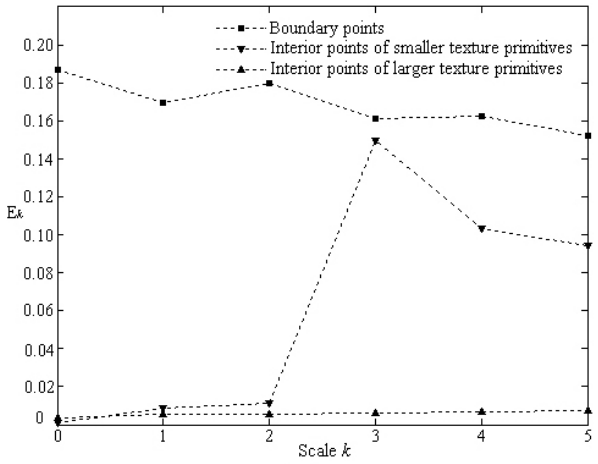

FIGURE 6. Typical curves of E_k varying with scale k.

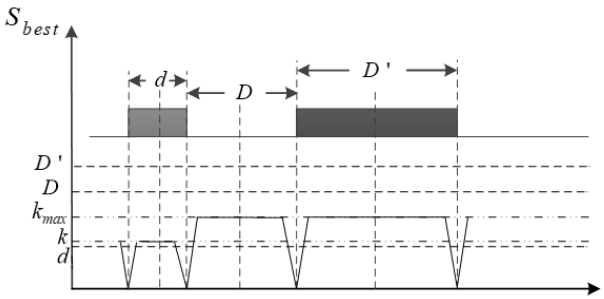

FIGURE 7. Scale k is discrete value, optimal size S_{best} output.

The curve of the pixel data point E_k of the experimental image varies with the scale k is shown in Fig. 6. The curve types can be roughly divided into three categories, corresponding to the boundary points, and the interior points of larger and smaller texture primitives.

In practical application, considering the time complexity, k is discrete, and L_{max} is not likely to be very large (usually 3-5). The actual output of S_{best} is shown in Fig. 7. Because of the discreteness of the internal point size of the same primitive, the S_{best} of the internal pixels has the same value. This does not contradict our coarseness measurement algorithm. On the contrary, it is reasonable that the pixels belonging to the same texture primitive have the same local coarseness.

Different primitives have different S_{best} due to different sizes. The larger size texture primitive S_{best} is obviously larger than the smaller texture. The S_{best} of larger texture primitives is obviously larger than that of smaller texture. Since L_{max} is small, for a smooth texture region of normal size (referring to non-point or only a few pixels), the output of texture region pixels is the largest S_{best}. At this time, we use the area with the largest pixel value in the coarseness feature map to measure the coarseness of this kind of texture. Obviously, the larger the area, the larger the coarseness of the corresponding texture. Therefore, we can distinguish different textures through the coarseness feature map. The

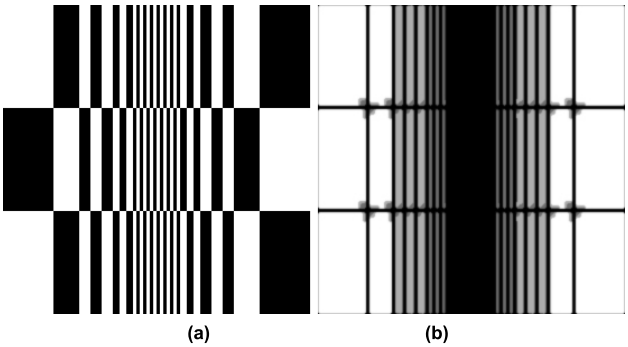

FIGURE 8. Artificial image experiment results. (a) Original image. (b) DTC coarseness feature map.

TABLE 2. Partial data of the ideal parabolic surface and datum.

Actual value	Extracted value	Relative error
91.5360	91.9022	0.4%
92.0790	91.9869	0.1%
91.7190	91.6336	0.12%
99.7440	99.8237	0.08%
100	99.8501	0.15%
97.6960	97.8209	0.13%

experimental results of Fig. 8 artificial image prove it. Each rectangular block in the original image (Fig. 8(a)) is equivalent to a texture primitive. Compared with the original image and its coarseness feature map (Fig. 8(b)), we can find that the larger the rectangular block, the larger the pixel value of the corresponding region in the coarseness feature map. When the size of the rectangular block is increased to a certain value, the pixel value of the corresponding area in the feature map reaches the maximum value, and the maximum rectangular block corresponding to the maximum pixel value area in the feature map is significantly larger than the sub-maximum rectangle.

C. ALGORITHM SIMULATION EXPERIMENT

In Fig. 9(a), the ideal parabolic surface is established according to the contour of the weld, and noise is added to simulate the actual weld surface. Then Gaussian filtering is performed to obtain the datum surface, and finally the roughness surface is separated, which is shown in Fig. 9(b).

At the same time, as we get the datum surface, we can use the obtained data to verify the accuracy of Gaussian filtering compared with the ideal parabolic surface generated. the maximum error of the ideal parabolic surface and the datum surface is 0.47%. The following table shows some data of the ideal paraboloid and the reference face ratio. We can know that the Gaussian filter in this paper is effective in extracting the datum.

The traditional Tamura algorithm and DTC algorithm are used to measure the roughness of the isolated roughness surface. The following Fig. 10 shows the S_{best} distribution obtained by the two algorithms. Ignoring the image boundary,

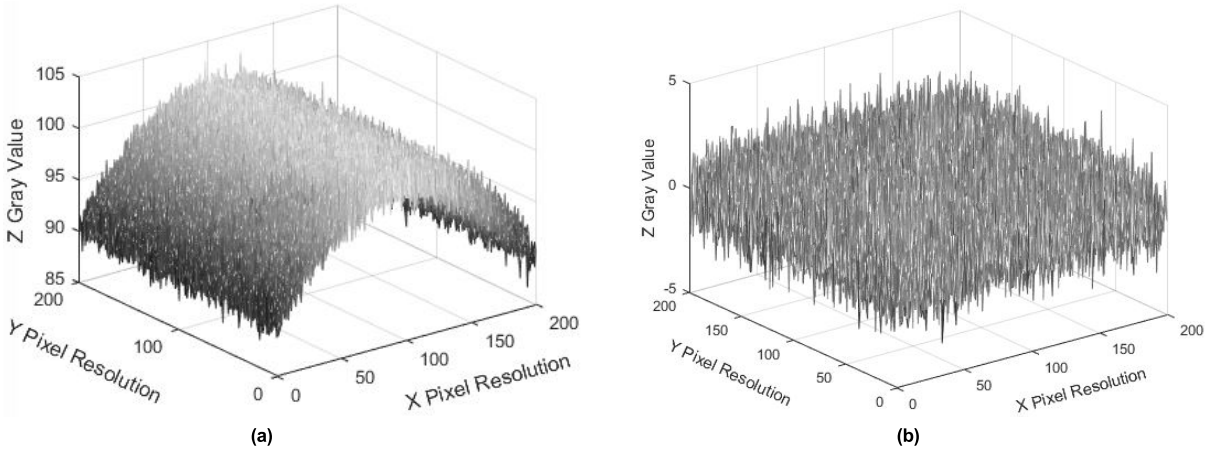

FIGURE 9. 3-D model of noisy surface and roughness surface. (a) Noise-carrying surface. (b) Roughness surface.

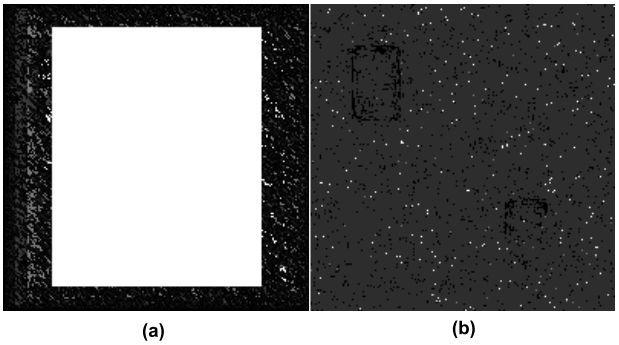

FIGURE 10. Separated roughness surface. (a) S_{best} of Tamura algorithm. (b) S_{best} of DTC algorithm.

there is no change in the S_{best} obtained by the Tamura algorithm in Fig. 10(a). It can be seen that the Tamura algorithm cannot recognize the local coarseness variation of the original roughness surface, and cannot detect the fine difference of the roughness surface texture sensitively. The DTC algorithm detects the local texture changes of the original roughness surface, which can accurately measure the local texture coarseness, which is of great significance for evaluating the roughness of the weld.

IV. EXPERIMENTAL RESULTS

A. ROUGHNESS COMPARISON SPECIMENS VERIFICATION EXPERIMENT

In this paper, we first compare the separability of texture coarseness of the algorithm on the roughness comparison specimens of Fig. 11.

Four kinds of roughness grades (Ra = 6.3, 25, 100, 800) of the above figure are scanned by structured light to obtain the contour, then the contour is filtered to obtain the roughness surface, and then the traditional mechanical industry 3-D roughness measurement value, texture feature parameters and dynamic texture coarseness are obtained respectively. The 3-D roughness of the mechanical industry generally refers to

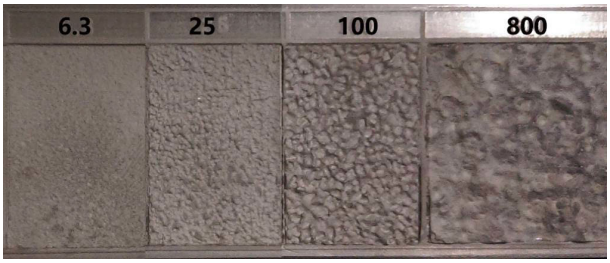

FIGURE 11. Roughness comparison specimens.

the contour arithmetic mean deviation S_a. S_a is the arithmetic mean of the linear distance from all the pixels on the measured surface to the corresponding points on the evaluation reference surface, and let $l(i, j)$ be any pixel point on the surface contour to the straight line distance of the corresponding point on the reference plane, there will be

$$S_a = \sqrt{\frac{1}{MN}\sum_{j=1}^{N}\sum_{i=1}^{M}|l(i,j)|} \tag{19}$$

The six elements in the image texture feature are average gray level, average contrast, smoothness, third moment, consistency, and entropy. The third moment reflects the measurement of histogram skewness. Entropy reflects the randomness of the pixels. The larger the skew, the coarser it is.

When scanning the roughness comparison specimens of a certain level, a large amount of contour data can be collected at one time, and the data can be segmented and tested. Multiple sets of roughness parameters can be obtained for the same specimens in different regions, and the stability of the algorithm can be verified by multiple measurements. The results are shown in Fig. 12.

It can be seen that using the arithmetic mean deviation of 3-D contour in mechanical industry to evaluate the roughness can distinguish the rougher surface better, but it cannot classify the smoother surface effectively, which is not conducive

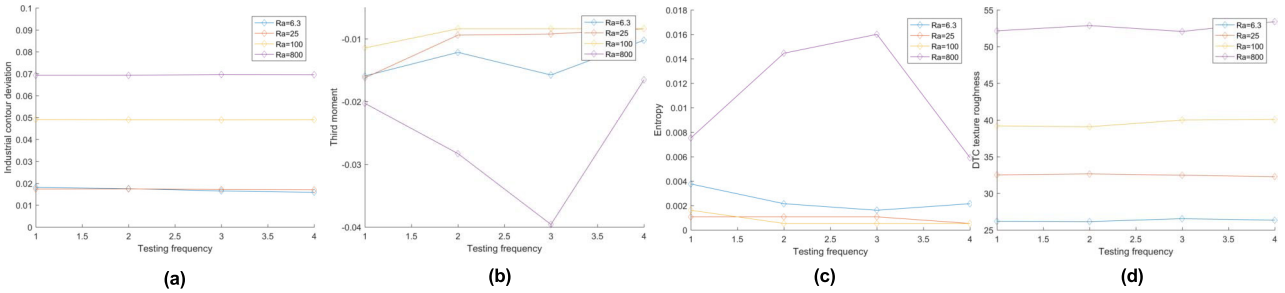

FIGURE 12. Comparison of roughness test results of specimens. (a) Industrial contour deviation Sa. (b) Third moment. (c) Entropy. (d) DTC texture roughness.

to the effective measurement of the 3-D roughness of the weld material surface; As for the components of the image texture feature: third moment, entropy. These two components have significant fluctuations when testing rougher surfaces, and they are not well differentiated for relatively smooth roughness; For the DTC algorithm, although the surface of the comparison specimens itself is concave and convex. The non-uniformity will cause the numerical fluctuation of texture roughness, but it still has stable separability for these four kinds of roughness grades. It can be used to judge the roughness of the weld.

B. OPTIMUM POSITION EXPERIMENT OF STRUCTURED LIGHT

The device of structured light is fixed behind the welding torch's forward direction, and the light is projected on the weld seam. The system continuously gives the roughness of the known weld seam on-line during the process of following the welder's advance. As shown in Fig. 13, the weld pool is near the bottom of the torch. The farther the structured light is from the molten pool portion, the more lagged the information of weld roughness is. However, the closer the light is to the molten pool, the greater the interference of arc light and high-brightness molten pool on the extraction of line structured light, or even the inaccurate extraction of the central line information of the weld contour. Therefore, experiments are needed to determine the optimal distance between the light and the center of the torch to ensure the balance between the extraction of the central line and the calculation of roughness.

The entire experimental setup includes intelligent welding robot; FRONIUS CMT Advanced 4000Rnc welding power source; protective air supply system; welding workbench; high nitrogen steel welding wire; 304 stainless steel base material; 3-D reconstruction system of structural light scanning, etc. High nitrogen steel wire is used in welding. The protective gas composition is 98.5% argon + 1.5% oxygen. The welding current is 130A, the shielding gas flow rate is 25L/min, and the welding speed is 30cm/min. By changing the position of the line structured light in the welding seam, the best position of the light distance from the center of the torch is determined by the quality of the light and the images

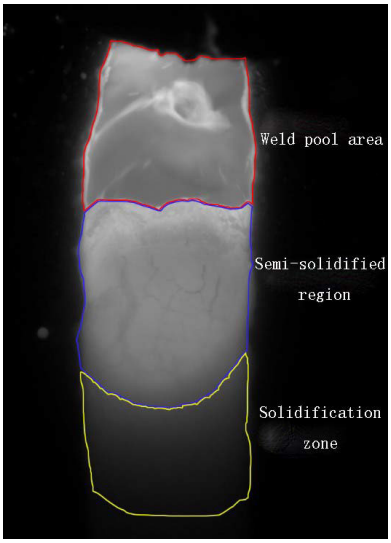

FIGURE 13. Weld state diagram for real-time acquisition.

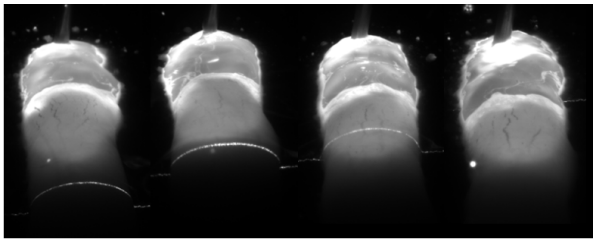

FIGURE 14. Diagram of line at different weld positions.

of the welding seam collected by the camera and the data analysis.

Firstly, the line laser is projected at a distance of 20 mm from the center of the center of the welding torch. The state of weld and line collected during welding are as shown in Fig. 14(a). Then the distance between the line and the wire is continuously shortened with the same welding parameters, and the other three weld states are obtained as shown in Fig. 14(b), (c)and (d).

For the case of 14(a), projection in solidified zone of weld, the obtained structured light image can extract the contour

FIGURE 15. Welds of different roughness grades. (a) Smooth. (b) Rough 1. (c) Rough 2. (d) Very rough 1. (e) Very rough 2.

section of weld well, and then obtain 3-D coordinates for the evaluation of weld roughness. However, the projection is 20 mm away from the weld wire, it makes the time lag of the obtained weld surface roughness relatively large, which is not conducive to timely discovery of welding problems. In view of Fig. 14(b), the line is pushed to the junction of semi-solidified region and solidified region, and the shape obtained is clear, which is conducive to extracting the center line of the light strip. Moreover, the profile projected by line laser at the junction is consistent with that of solidified weld seam, which can provide accurate roughness information. Then push the structured light forward to the semi-solidified area as shown in Fig. 14(c). It can be seen that the line in the semi-solidified area is no longer clear because of the overlap with the background of the semi-solidified weld, which is not conducive to the extraction of the light. For the state of Fig. 14(d), the laser is projected on the molten pool. The molten pool is a liquid metal part with a certain geometric shape. Since the laser is applied to the liquid metal, most of the light is emitted by the mirror surface, so it cannot be collected by the camera. Secondly, the surface fluidity of the molten pool makes the molten pool and solidified weld have completely different appearance. Therefore, the position of Fig. 14(d) is not suitable for on-line roughness calculation.

In summary, the optimal position of the line structured light distance from the wire in the 3-D roughness system is at the junction of the semi-solidified and solidified zone of the weld, where the structured light is easy to handle, and the roughness of the welded zone can also be given with low delay.

C. ON-LINE WELDING QUALITY TESTING

Different welding types, wire materials and welding parameters, the surface roughness obtained in the welding will also be different. The following welds with different roughness grades are produced by adjusting the welding conditions, structured light is projected to the junction of semi-solidification and solidification zone of the weld to verify the algorithm online. Five groups of welds with different roughness levels are shown in Fig. 15. (a) smooth, (b), (c) rough, (d) (e) very rough.

During the welding process, the roughness of these welds under different welding conditions is judged by the roughness measurement system in this paper. At the same time, we choose the industrial roughness which is relatively good

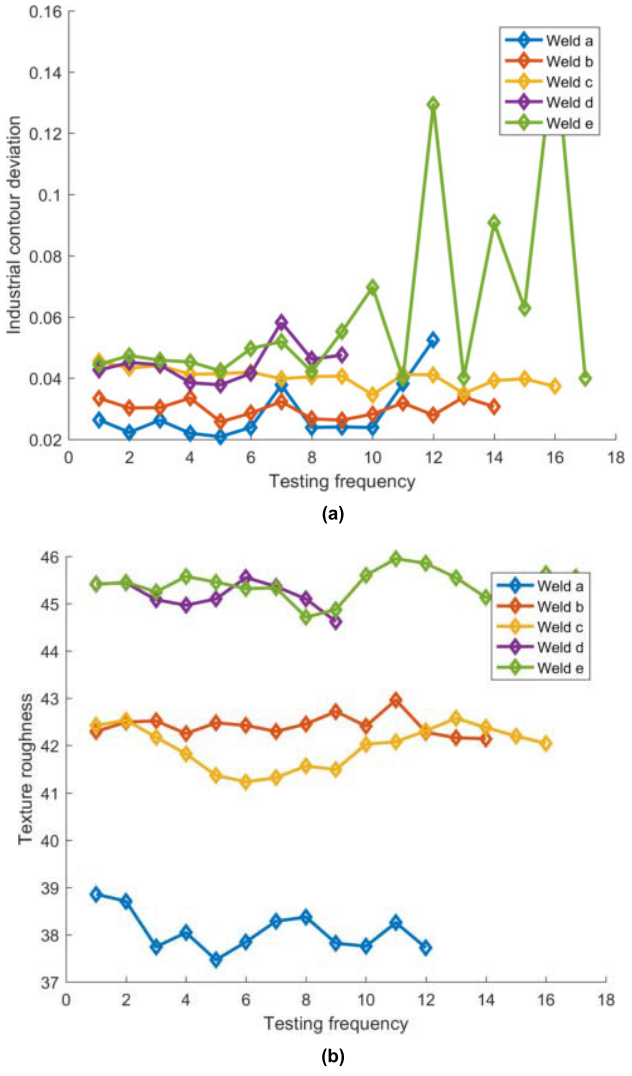

FIGURE 16. Distribution of weld roughness. (a) Industrial contour deviation Sa. (b) DTC texture roughness.

in the experiment of standard specimens to compare. The experimental results are shown in Fig. 16.

The length of each weld is different, so the number of weld segments is different. It can be seen from the result graph that industrial parameters still cannot accurately classify weld roughness and our algorithm has obvious effect on the classification of roughness, which can distinguish the three grades of smooth, rough and very rough, and the classification of different welds in the same grade and the division of different areas of the same weld. The segment test shows that the roughness classification results are stable and have very effective classification characteristics.

V. CONCLUSION

1) In this paper, a 3-D reconstruction system based on structured light is established. The 3-D contour of the weld surface is obtained for the calculation of roughness by using the

characteristics of good light pattern, strong directivity and high strength.

2) The optimum distance between the structured light and the center of the torch is determined through the experiment of continuously changing the distance between the line and the welding wire, which ensures the balance between the extraction of the contour centerline and the low delay of the roughness calculation.

3) Combining 2-D Gaussian filtering and texture coarseness, a dynamic texture coarseness algorithm is proposed. The DTC algorithm is applied to the low-delay online evaluation of the roughness of additive. The algorithm is validated by roughness comparison specimens and actual welds. The classification results are credible and meet the evaluation criteria of weld quality.

ACKNOWLEDGMENT

(Haotian Yu and Chongchong Peng are co-first authors.)

REFERENCES

[1] B. Liu, Q. Feng, and Z. Kuang, "Summary of surface roughness measurement methods," *Opt. Instrum.*, vol. 26, no. 5, pp. 54–58, 2004.

[2] H. Hou, Y. Kui, J. Shao, and Z. Fan, "An instrument for surface roughness measurement of optical thin films," *Proc. SPIE*, vol. 5638, no. 2, pp. 638–642, Feb. 2005.

[3] S. Li, Q. Yuan, L. Xu, J. Xing, W. Liu, Z. Gao, and L. Shi, "Image detection algorithm for cutting surface roughness of grape hard branch grafting based on light-section method," *Trans. Chin. Soc. Agricult. Eng.*, vol. 33, no. 4, pp. 234–241, Feb. 2017.

[4] B. He and S. Ding, "Summary of 3-D surface roughness measurement methods," *Opt. Precis. Eng.*, vol. 27, no. 1, pp. 78–93, 2019.

[5] Y. Zhang and T. Cui, "Research on 3-D measurement and evaluation of surface roughness," *Meas. Meas. Technol.*, vol. 39, no. 11, pp. 31–32, 2012.

[6] D. J. Whitehouse, "Profile and areal (3-D) parameter characterization," in *Surface Their Measurement*, Cleveland, OH, USA: Penton, 2002, pp. 50–62.

[7] J. YANG, J. LU, and J. WANG, "Design of 3-D roughness instrument with stylus," *Machinery Design Manuf.*, vol. 39, no. 11, p. 34. 2012.

[8] B. Moralejo A. Tejero V. Hortelano O. Martínez, M. A. González, and J. Jiménez, "Defect recognition by means of light and electron probe techniques for the characterization of mc-Si wafers and solar cells," *Superlattices Microstruct.*, vol. 99, pp. 45–53, Nov. 2016.

[9] Y. Q. Wang, D. Tian, D. Y. Song, and L. Zhang, "Application of improved invariant moments and SVM in the recognition of solar cell defects," *Appl. Mech. Mater.*, vols. 672–674, pp. 3–6, Oct. 2014.

[10] X. Liu, S. Huang, and T. Liu, "Study on image acquisition and processing of CO2 welding pool," in *Proc. Shandong Ind. Technol.*, 2016, pp. 28–29.

[11] Y. He, Y. Xu, Y. Chen, and S. Chen, "Weld seam profile detection and feature point extraction for multi-pass route planning based on visual attention model," *Robot. Comput.-Integr. Manuf.*, vol. 37, pp. 251–261, Feb. 2016.

[12] X. Ma and Y. Zhang, "Gas metal arc weld pool surface imaging modeling and processing," *Welding J.*, vol. 90, no. 5, pp. 85s–94s, May 2011.

[13] D. Lin, "Research on the ship weld defect recognition system based on the computer vision," *Ship Sci. Technol.*, vol. 40, no. 2, pp. 212–214, 2018.

[14] J. Yang, Z. Li, L. Fan, and Q. Huang, "Weld surface defect detection system based on line laser scanning," *Weld. Joining*, no. 2, pp. 19–23, 2016.

[15] L. I. Zhao-Tai, W. Cheng-Sen, and H. Zhi, "Ultrasonic testing for the process piping butt weld," *Nondestruct. Test.*, vol. 33, no. 8, p. 46, 2011.

[16] H. Tamura, S. Mori, and T. Yamawaki, "Textural features corresponding to visual perception," *IEEE Trans. Syst., Man, Cybern.*, vol. SMC-8, no. 6, pp. 460–473, Jun. 1978.

[17] *Geometrical Product Specifications (GPS)-Surface Texture: ArealPart 6: Classification of Methods for Measuring Surface Texture International Organization of Standardization*, ISO Standard 25178-6, International Organization for Standardization, Geneva, Switzerland, 2010.

[18] *General Administration of Quality Supervision, Inspection and Quarantine of the People's Republic of China. Standardization Administration of China. Geometrical Product Specifications (GPS)-Surface Texture: Areal-Part 6: Classification of Methods for Measuring Surface Texture*, Standard GB/T33523.6-2017, Standards Press of China, Beijing, China, 2017.

[19] T. Luhmann, S. Robson, and S. Kyle, "Digital image processing," in *Close Range Photogrammetry: Principles, Techniques and Applications*, New York, NY, USA: Wiley, 2006, pp. 378–397.

[20] C. Stachniss, J. J. Leonard, and S. Thrun, *Simultaneous Localization and Mapping*. Cham, Switzerland: Springer, 2016, pp. 1153–1176.

[21] G. Younes, D. Asmar, E. Shammas, and J. Zelek, "Keyframe-based monocular SLAM: Design, survey, and future directions," *Robot. Auto. Syst.*, vol. 98, pp. 67–88, Dec. 2017.

[22] R. Gomez-Ojeda, F. A. Moreno, D. Scaramuzza, and J. Gonzalez-Jimenez, "PL-SLAM: A stereo SLAM system through the combination of points and line segments," *IEEE Trans. Robot.*, to be published.

[23] T. Whelan, M. Kaess, H. Johannsson, M. Fallon, J. J. Leonard, and J. McDonald, "Real-time large-scale dense RGB-D SLAM with volumetric fusion," *Int. J. Robot. Res.*, vol. 34, nos. 4–5, pp. 598–626, Apr. 2015.

[24] Y. Sun, M. Liu, and M. Q.-H. Meng, "Motion removal for reliable RGB-D SLAM in dynamic environments," *Robot. Auto. Syst.*, vol. 108, pp. 115–128, Oct. 2018.

[25] Y. Sun, M. Liu, and M. Q.-H. Meng, "Improving RGB-D SLAM in dynamic environments: A motion removal approach," *Robot. Auto. Syst.*, vol. 89, pp. 110–122, Mar. 2017.

[26] N. Snavely, S. M. Seitz, and R. Szeliski, "Photo tourism: Exploring photo collections in 3-D," *ACM Trans. Graph.*, vol. 25, no. 3, pp. 835–846, Jul. 2006.

[27] C. Wu, "Towards linear-time incremental structure from motion," in *Proc. Int. Conf. 3D*, Jun. 2013, pp. 127–134.

[28] J. L. Schönberger and J. M. Frahm, "Structure-from-motion revisited," in *Proc. IEEE Conf. Comput. Vis. Pattern Recognit. (CVPR)*, Jun. 2016, pp. 4104–4113.

[29] Z. Zhang, "A flexible new technique for camera calibration," *IEEE Trans. Pattern Anal. Mach. Intell.*, vol. 22, no. 11, pp. 1330–1334, Dec. 2000.

[30] K. Yang, H. Y. Yu, and C. Yang, "Calibration of line structured-light vision measurement system based on free-target," *J. Mech. Electr. Eng.*, vol. 33, no. 9, pp. 1066–1070, 2016.

[31] G. Genta, P. Minetola, and G. Barbato, "Calibration procedure for a laser triangulation scanner with uncertainty evaluation," *Opt. Lasers Eng.*, vol. 86, pp. 11–19, Nov. 2016.

[32] E. Seneta, "On the history of the strong law of large numbers and Boole's inequality," *Hist. Math.*, vol. 19, no. 1, pp. 24–39, 1992.

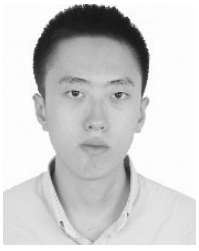

HAOTIAN YU received the B.S. degree in electronic science and technology and the M.S. degree in optical engineering from the Nanjing University of Science and Technology, in 2016 and 2018, respectively, where he is currently pursuing the Ph.D. degree. His research interests include computer vision, sensors, and 3-D reconstruction.

CHONGCHONG PENG received the B.S. degree in electronic science and technology from the Nanjing University of Science and Technology, in 2017, where he is currently pursuing the M.S. degree in optical engineering. His research interests include computer vision, sensors, 3-D reconstruction, and deep learning.

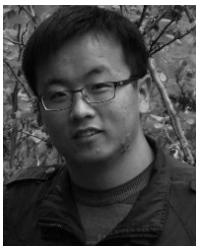

ZHUANG ZHAO received the B.S. degree in electronic science and technology, the M.S. degree in optical engineering, and the Ph.D. degree from the Nanjing University of Science and Technology, in 2009, 2013, and 2019, respectively, where he is currently a Lecturer. His research interests include computer vision, sensors, and spectral analysis.

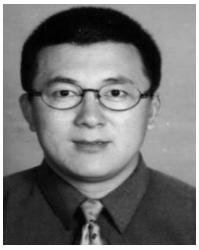

LIANFA BAI received the Ph.D. degree from the Nanjing University of Science and Technology, in 1995, where he is currently a Professor. His research interests include photoelectric detection and imaging, photoelectric information (image) processing, transmission, and display.

JING HAN received the B.S. degree in electronic science and technology, the M.S. degree in optical engineering, and the Ph.D. degree from the Nanjing University of Science and Technology, in 2009, 2012, and 2015, respectively, where she is currently an Associate Professor. Her research interests include computer vision, sensors, and image segmentation.